Illumination compensation for subsalt image-domain wavefield tomography

Tongning Yang, Center for Wave Phenomena, Colorado School of Mines,*
Jeffrey Shragge, School of Earth and Environment, University of Western Australia,
and Paul Sava, Center for Wave Phenomena, Colorado School of Mines

SUMMARY

Wavefield tomography represents a family of velocity model building techniques based on seismic waveforms as the input and seismic wavefields as the information carrier. For wavefield tomography implemented in the image domain, the objective function is designed to optimize the coherency of reflections in extended common-image gathers. This function applies a penalty operator to the gathers, thus highlighting image inaccuracies due to the velocity model error. Uneven illumination is a common problem for complex geological regions, such as subsalt. Imbalanced illumination results in defocusing in common-image gathers regardless of the velocity model accuracy. This additional defocusing violates the wavefield tomography assumption stating that the migrated images are perfectly focused in the case of the correct model and degrades the model reconstruction. We address this problem by incorporating the illumination effects into the penalty operator such that only the defocusing due to model errors is used for model construction. This method improves the robustness and effectiveness of wavefield tomography applied in areas characterized by poor illumination. The Sigsbee synthetic example demonstrates that velocity models are more accurately reconstructed by our method using the illumination compensation, leading to more coherent and better focused subsurface images than those obtained by the conventional approach without illumination compensation.

INTRODUCTION

Building an accurate and reliable velocity model remains one of the biggest challenges in current seismic imaging practice. In regions characterized by complex subsurface structure, prestack wave-equation depth migration, (e.g., one-way wave-equation migration or reverse-time migration), is a powerful tool for accurately imaging the earth's interior (Gray et al., 2001; Etgen et al., 2009). The widespread use of these advanced imaging techniques drives the need for high-quality velocity models because these methods are very sensitive to model errors (Symes, 2008; Woodward et al., 2008; Virieux and Operto, 2009).

Wavefield tomography represents a family of techniques for velocity model building using seismic wavefields (Tarantola, 1984; Woodward, 1992; Pratt, 1999; Sirgue and Pratt, 2004; Plessix, 2006; Vigh and Starr, 2008; Plessix, 2009). The core of wavefield tomography is using a wave equation (typically constant density acoustic) to simulate wavefields as the information carrier. Wavefield tomography is usually implemented in the data domain by adjusting the velocity model such that simulated and recorded data match (Tarantola, 1984; Pratt, 1999). This match is based on the strong assumption that the wave equation used for simulation is consistent with the physics of the earth. However, this is unlikely to be the case when the earth is characterized by strong (poro)elasticity. Significant effort is often directed toward removing the components of the recorded data that are inconsistent with the assumptions used.

Wavefield tomography can also be implemented in the image domain rather than in the data domain. Instead of minimizing the data misfit, the techniques in this category update the velocity model by optimizing the image quality (Yilmaz, 2001). Differential semblance optimization (DSO) is one realization of image-domain wavefield tomography (Symes and Carazzone, 1991). The essence of the method is to minimize the difference between same reflection observed at neighboring offsets or angles (Shen and Calandra, 2005; Shen and Symes, 2008). DSO implemented using space-lag gathers constructs a penalty operator which annihilates the energy at zero lag and enhances the energy at nonzero lags (Shen et al., 2003). This construction assumes that migrated images are perfectly focused at zero lag when the model is correct. This assumption, however, is violated in practice when the subsurface illumination is uneven. In complex subsurface regions, such as subsalt, uneven illumination is a general problem and it deteriorates the quality of imaging and velocity model building (Leveille et al., 2011). Several approaches have been proposed for illumination compensation of imaging (Gherasim et al., 2010; Shen et al., 2011), but not for velocity model building. In this paper, we address the problem of uneven illumination associated with image-domain wavefield tomography. The main idea is to include the illumination information in the penalty operator used by the objective function such that the defocusing due the illumination is excluded from the model updating process. We illustrate our technique with a subsalt velocity model.

THEORY

The core element for image-domain wavefield tomography using space-lag extended images (subsurface-offset CIGs) is an objective function and its gradient computed using the adjoint-state method (Plessix, 2006; Symes, 2009). The state variables relate the objective function to the model parameter and are defined as source and receiver wavefields u_s and u_r obtained by solving the following acoustic wave equation:

$$\begin{bmatrix} \mathcal{L}\left(\mathbf{x},\omega,m\right) & 0 \\ 0 & \mathcal{L}^{*}\left(\mathbf{x},\omega,m\right) \end{bmatrix} \begin{bmatrix} u_s\left(j,\mathbf{x},\omega\right) \\ u_r\left(j,\mathbf{x},\omega\right) \end{bmatrix} = \begin{bmatrix} f_s\left(j,\mathbf{x},\omega\right) \\ f_r\left(j,\mathbf{x},\omega\right) \end{bmatrix}, \tag{1}$$

where $\mathcal{L}$ and $\mathcal{L}^{*}$ are forward and adjoint frequency-domain wave operators, f_s and f_r are the source and record data, $j = 1, 2, ..., N_s$ where N_s is the number of shots, ω is the angular frequency, and $\mathbf{x}$ are the space coordinates $\{x, y, z\}$. The wave operator $\mathcal{L}$ and its adjoint $\mathcal{L}^{*}$ propagate the wavefields

forward and backward in time respectively using a two-way wave equation, e.g., $\mathcal{L} = -\omega^2 m - \Delta$, where m represent slowness squared. The objective function for image-domain wavefield tomography measures the image incoherency caused by the model errors

$$\mathcal{H}_{\boldsymbol{\lambda}} = \frac{1}{2} \| K_I\left(\mathbf{x}\right) P\left(\boldsymbol{\lambda}\right) r\left(\mathbf{x}, \boldsymbol{\lambda}\right) \|^2_{\mathbf{x},\boldsymbol{\lambda}} \ , \tag{2}$$

where $r\left(\mathbf{x}, \boldsymbol{\lambda}\right)$ are extended images:

$$r\left(\mathbf{x}, \boldsymbol{\lambda}\right) = \sum_j \sum_\omega \overline{u_s\left(j, \mathbf{x} - \boldsymbol{\lambda}, \omega\right)} u_r\left(j, \mathbf{x} + \boldsymbol{\lambda}, \omega\right) \ , \tag{3}$$

The overline represents complex conjugate, and the lag vector has, in this case, only horizontal components: $\boldsymbol{\lambda} = \{\lambda_x, \lambda_y, 0\}$. The mask operator $K_I\left(\mathbf{x}\right)$ limits the construction of the gathers to select locations in the subsurface. $P\left(\boldsymbol{\lambda}\right)$ is a penalty operator acting on the extended image to highlight defocusing, i.e. image inaccuracy. It is typically assumed that defocusing is only due to velocity error, an assumption which leads to the differential semblance optimization (DSO) operator of Symes (2008). However, this penalty operator is not effective when poor illumination affects the image accuracy and leads to additional defocusing.

To alleviate the negative influence of poor illumination, we need to include the illumination distribution in the tomographic procedure. Illumination can be assessed by applying illumination analysis, which is formulated based on the migration deconvolution, given by the expression

$$\tilde{r}\left(\mathbf{x}\right) = \left(\mathcal{M}^* \mathcal{M}\right)^{-1} r\left(\mathbf{x}\right) \ , \tag{4}$$

where $\tilde{r}$ is a reflectivity distribution, r is a migrated image, $\mathcal{M}$ is a demigration operator which is linear with respect to the reflectivity. This operator is different from the modeling operator $\mathcal{L}$. The adjoint $\mathcal{M}^*$ represents the migration operator. $(\mathcal{M}^* \mathcal{M})$ is a blurring operator, and represents the Hessian (second-order derivative of the operator with respect to the model) for the operator $\mathcal{M}$. This term includes the subsurface illumination information associated with the velocity structure and the acquisition geometry. In practice, the full $(\mathcal{M}^* \mathcal{M})^{-1}$ matrix is too costly to construct, but we can evaluate its impact by applying a cascade of demigration and migration $(\mathcal{M}^* \mathcal{M})$ to a reference image. For example, using extended images, we can write:

$$r_e\left(\mathbf{x}, \boldsymbol{\lambda}\right) = \mathcal{M}^* \mathcal{M} r\left(\mathbf{x}, \boldsymbol{\lambda}\right) \ . \tag{5}$$

The resulting image r_e approximates the diagonal elements of the Hessian and captures defocusing associated with illumination effects. Such defocusing is the consequence of uneven illumination and should not be used in the velocity update. Therefore, an illumination-based penalty operator can be constructed as

$$P\left(\mathbf{x}, \boldsymbol{\lambda}\right) = \frac{1}{E[r_e\left(\mathbf{x}, \boldsymbol{\lambda}\right)] + \epsilon} \ , \tag{6}$$

where E represents envelope and ϵ is a damping factor used to stabilize the division. Replacing the conventional penalty $P = |\boldsymbol{\lambda}|$ with the one in equation 6 is the basis for our illumination compensated image-domain wavefield tomography. Note that the DSO penalty operator is a special case of our new penalty operator and corresponds to the case of perfect subsurface illumination and wide-band data.

The adjoint sources are computed as the derivatives of the objective function $\mathcal{H}_{\boldsymbol{\lambda}}$ shown in equation 2 with respect to the state variables u_s and u_r:

$$\begin{bmatrix} g_s\left(j, \mathbf{x}, \omega\right) \\ g_r\left(j, \mathbf{x}, \omega\right) \end{bmatrix} = \begin{bmatrix} \sum\limits_{\boldsymbol{\lambda}} P\left(\boldsymbol{\lambda}\right) \ K_I\left(\mathbf{x}\right) \overline{K_I\left(\mathbf{x}\right) P\left(\boldsymbol{\lambda}\right) r\left(\mathbf{x}, \boldsymbol{\lambda}\right)} u_r\left(j, \mathbf{x} + \boldsymbol{\lambda}, \omega\right) \\ \sum\limits_{\boldsymbol{\lambda}} P\left(\boldsymbol{\lambda}\right) \ K_I\left(\mathbf{x}\right) \overline{K_I\left(\mathbf{x}\right) P\left(\boldsymbol{\lambda}\right)} r\left(\mathbf{x}, \boldsymbol{\lambda}\right) u_s\left(j, \mathbf{x} - \boldsymbol{\lambda}, \omega\right) \end{bmatrix} . \tag{7}$$

The adjoint state variables a_s and a_r are the wavefields obtained by backward and forward modeling, respectively, using the corresponding adjoint sources defined in equation 7:

$$\begin{bmatrix} \mathcal{L}^*\left(\mathbf{x}, \omega, m\right) & 0 \\ 0 & \mathcal{L}\left(\mathbf{x}, \omega, m\right) \end{bmatrix} \begin{bmatrix} a_s\left(j, \mathbf{x}, \omega\right) \\ a_r\left(j, \mathbf{x}, \omega\right) \end{bmatrix} = \begin{bmatrix} g_s\left(j, \mathbf{x}, \omega\right) \\ g_r\left(j, \mathbf{x}, \omega\right) \end{bmatrix} \ , \tag{8}$$

and the gradient is the correlation between state variables and adjoint state variables:

$$\frac{\partial \mathcal{H}_{\boldsymbol{\lambda}}}{\partial m} = \sum_j \sum_\omega \frac{\partial \mathcal{L}}{\partial m} \left(u_s\left(j, \mathbf{x}, \omega\right) \overline{a_s\left(j, \mathbf{x}, \omega\right)} + u_r\left(j, \mathbf{x}, \omega\right) \overline{a_r\left(j, \mathbf{x}, \omega\right)} \right) \ , \tag{9}$$

The model is then updated using gradient line search aimed at minimizing the objective function given by equation 2.

EXAMPLES

In this section, we use the Sigsbee 2A model (Paffenholz et al., 2002) and concentrate on the subsalt area to test our method in regions of complex geology with poor illumination. The target area ranges from $x = 6.5 - 20$ km, and from $z = 4.5 - 9$ km. The model, migrated image, and angle-domain gathers for correct and initial models are shown in Figures 1(a)-1(c) and Figures 2(a)-2(c), respectively. The angle gathers are displayed at selected locations corresponding to the vertical bars overlain in Figure 1(b). The actual spacing of the gathers and penalty operators are 0.45 km. Note that the reflections in the angle gathers appear only at positive angles, as the data are simulated for towed streamers and the subsurface is illuminated from one side only. We run the inversion using both the conventional DSO penalty and the illumination-based penalty operators. The DSO penalty operator is shown in Figure 3(a). For the illumination-based operator, we first generate gathers containing defocusing due to illumination effects (Figure 3(b)), and then we construct the penalty operator using equation 6, as shown in Figure 3(c). For the gathers characterizing the illumination effects, we can observe significant defocusing in the subsalt area, as the salt distorts the wavefields used for imaging and causes the poor illumination.

We run both inversions for 10 iterations, and obtain the reconstructed model, migrated image, and angle-domain gath-

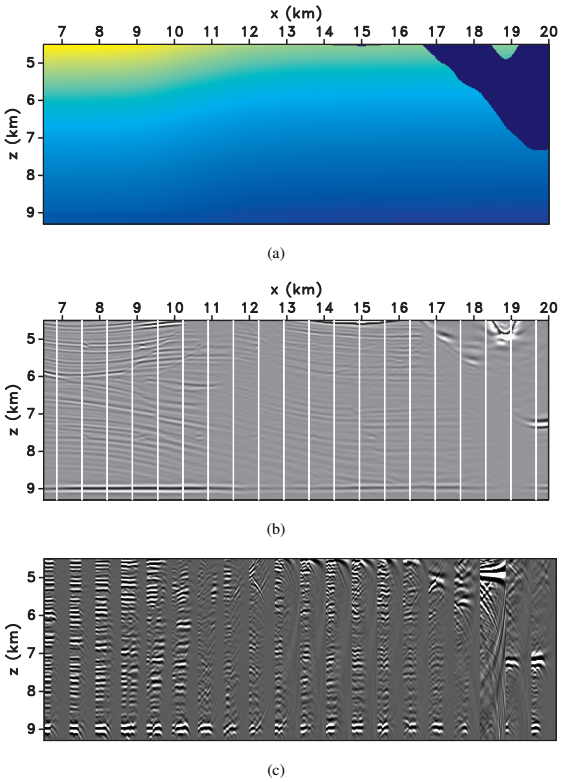

Figure 1: (a) The true model in the target area of the Sigsbee model. (b) The corresponding migrated image, and (c) the angle-domain gathers.

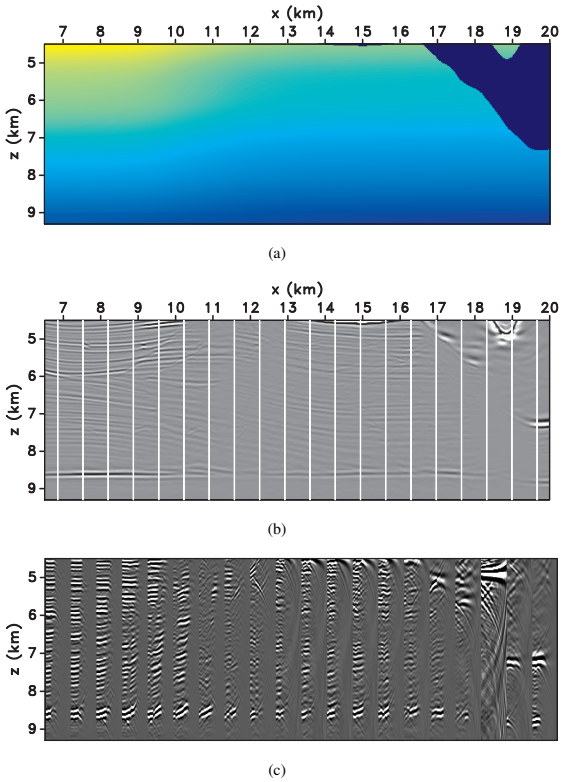

Figure 2: (a) The initial model obtained by scaling the subsalt sediments of the true model. (b) The corresponding migrated image, and (c) the angle-domain gathers.

ers shown in Figures 4(a)- 4(c) and Figures 5(a)-5(c), respectively. The figures show that we update the models in the correct direction in both cases and that the reconstructed models are closer to the true model than the starting model. We find, however, that the model obtained using the illumination-based penalty is closer to the true model than the model obtained using DSO penalty. The model obtained using DSO penalty is not sufficiently updated and is still too slow. This is because the severe defocusing due to the salt biases the inversion when we do not take into account the uneven illumination. The comparison of the images also suggests that the inversion using the illumination-based penalty is superior to the inversion using DSO penalty. Both images are improved due to the updated model, as illustrated by the better focused diffractors distributed at $z = 7.6$ km, and by the faults located between $x = 14.0$ km, $z = 6.0$ km and $x = 16.0$ km, $z = 9.0$ km which are more visible in the images. If we concentrate on the bottom reflector (around 9 km), we can distinguish the extent of the improvements on the image quality for both inversions. The bottom reflector is corrected to the right depth for inversion using the illumination-based penalty, while for inversion using the DSO penalty, this reflector is still misplaced from the correct depth and it is not as flat as the reflector in Figure 5(b). Figures 6(a)-6(d) compare the angle gathers at $x = 10.2$ km for the correct, initial, and reconstructed models using DSO and illumination-based penalties. The gathers for both reconstructed models show flatter reflections, indicating that the reconstructed models are more accurate than the

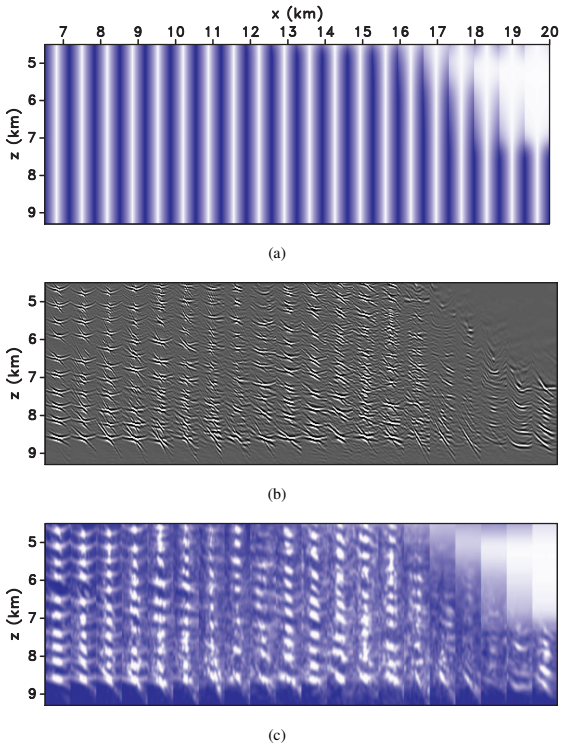

Figure 3: (a) The DSO penalty operator. (b) The gathers characterizing the illumination effects. (c) The illumination-based penalty operator constructed from the gathers in Figure 9(b).

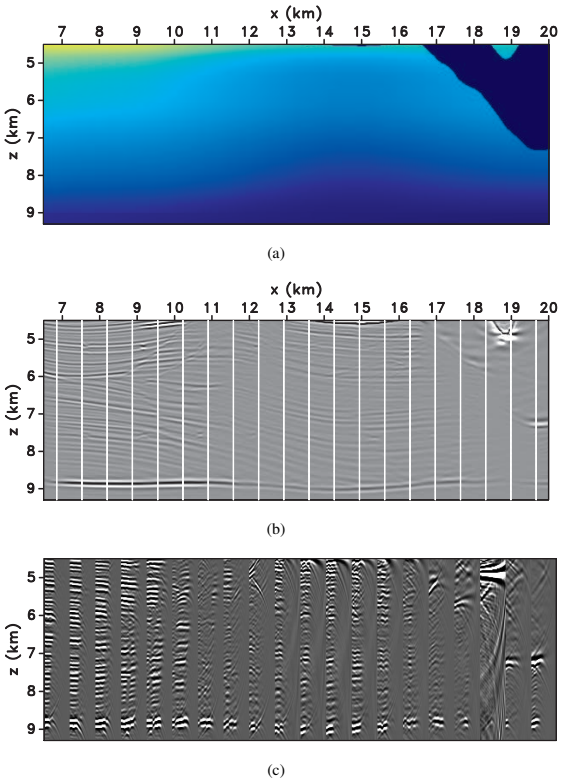

Figure 4: (a) The reconstructed model from inversion using the DSO penalty. (b) The corresponding migrated image, and (c) the angle-domain gathers.

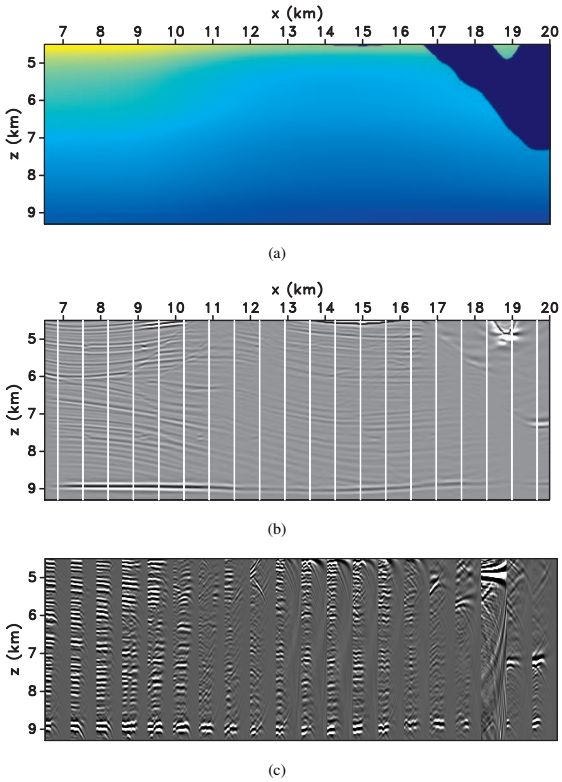

Figure 5: (a) The reconstructed model from inversion using the illumination-based penalty. (b) The corresponding migrated image, and (c) the angle-domain gathers.

initial model. We can, nonetheless, observe that the reflections in Figure 6(d) are flatter than those in Figure 6(c), and conclude that the reconstructed model using the illumination-based penalty is more accurate, since it accounts for the poor subsurface illumination.

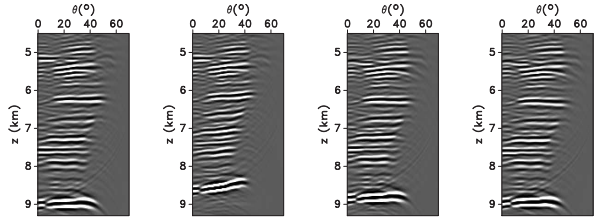

Figure 6: Angle-domain gathers at $x = 10.2$ km for (a) the correct model, (b) the initial model, the reconstructed models using (c) the DSO penalty, and (d) the illumination-based penalty.

CONCLUSIONS

We demonstrate an illumination compensation strategy for wavefield tomography in the image domain. The idea is to measure the illumination effects on space-lag extended images, and replace the conventional DSO penalty operator with another one that compensates for illumination. This workflow isolates the defocusing caused by the illumination such that image-domain wavefield tomography minimizes only the defocusing related to velocity error. The synthetic examples show the improvements of the inversion result and of the migrated image after the illumination information is included in the penalty operator. Our approach enhances the robustness and effectiveness of wavefield tomography in the model building process when the subsurface illumination is uneven due to complex geologic structures such as salt. The cost of this technique is higher than that of the conventional approach since we periodically need to re-evaluate the subsurface illumination.

ACKNOWLEDGMENTS

We acknowledge the support of the sponsors of the Center for Wave Phenomena at Colorado School of Mines. The reproducible numeric examples in this paper use the Madagascar open-source software package freely available from http://www.reproducibility.org.

REFERENCES

Etgen, J., S. H. Gray, and Y. Zhang, 2009, An overview of depth imaging in exploration geophysics: Geophysics, **74**, WCA5–WCA17.

Gherasim, M., U. Albertin, B. Nolte, and O. Askim, 2010, Wave-equation angle-based illumination weighting for optimized subsalt imaging: Presented at the 80th Annual International Meeting, SEG, Expanded Abstracts.

Gray, S. H., J. Etgen, J. Dellinger, and D. Whitmore, 2001, Seismic migration problems and solutions: Geophysics, **66**, 1622–1640.

Leveille, J. P., I. F. Jones, Z. Z. Zhou, B. Wang, and F. Liu, 2011, Subsalt imaging for exploration, production, and development: A review: Geophysics, **76**, WB3–WB20.

Paffenholz, J., B. McLain, J. Zaske, and P. Keliher, 2002, Subsalt multiple attenuation and imaging: Observations from the sigsbee 2b synthetic dataset: 72nd Annual International Meeting, SEG, Expanded Abstracts, 2122–2125.

Plessix, R.-E., 2006, A review of the adjoint state method for computing the gradient of a functional with geophysical applications: Geophysical Journal International, **167**, 495–503.

———, 2009, Three-dimensional frequency-domain full-waveform inversion with an iterative solver: Geophysics, **74**, WCC53–WCC61.

Pratt, R. G., 1999, Seismic waveform inversion in the frequency domain, Part 1: Theory and verification in a physical scale model: Geophysics, **64**, 888–901.

Shen, H., S. Mothi, and U. Albertin, 2011, Improving subsalt imaging with illumination-based weighting of rtm 3d angle gathers: Presented at the 81th Annual International Meeting, SEG, Expanded Abstracts.

Shen, P., and H. Calandra, 2005, One-way waveform inversion within the framework of adjoint state differential migration: 75th Annual International Meeting, SEG, Expanded Abstracts, 1709–1712.

Shen, P., C. Stolk, and W. Symes, 2003, Automatic velocity analysis by differential semblance optimization: 73th Annual International Meeting, SEG, Expanded Abstracts, 2132–2135.

Shen, P., and W. W. Symes, 2008, Automatic velocity analysis via shot profile migration: Geophysics, **73**, VE49–VE59.

Sirgue, L., and R. Pratt, 2004, Efficient waveform inversion and imaging: A strategy for selecting temporal frequencies: Geophysics, **69**, 231–248.

Symes, W., 2009, Migration velocity analysis and waveform inversion: Geophysical Prospecting, **56**, 765–790.

Symes, W. W., 2008, Migration velocity analysis and waveform inversion: Geophysical Prospecting, **56**, 765–790.

Symes, W. W., and J. J. Carazzone, 1991, Velocity inversion by differential semblance optimization: Geophysics, **56**, 654–663.

Tarantola, A., 1984, Inversion of seismic reflection data in the acoustic approximation: Geophysics, **49**, 1259–1266.

Vigh, D., and E. W. Starr, 2008, 3D prestack plane-wave, full-waveform inversion: Geophysics, **73**, VE135–VE144.

Virieux, J., and S. Operto, 2009, An overview of full-waveform inversion in exploration geophysics: Geophysics, **74**, WCC1–WCC26.

Woodward, M., D. Nichols, O. Zdraveva, P. Whitfield, and T. Johns, 2008, A decade of tomography: Geophysics, **73**, VE5–VE11.

Woodward, M. J., 1992, Wave-equation tomography: Geophysics, **57**, 15–26.

Yilmaz, O., 2001, Seismic Data Analysis (2nd edition): Society of Exploration Geophysicists.